

## Phosphors with different morphology, formed under hydrothermal conditions on the basis of $\text{ZrO}_2:\text{Eu}^{3+}$ nanocrystallites

A. N. Bugrov<sup>1,2</sup>, R. Yu. Smyslov<sup>1,3</sup>, T. V. Khamova<sup>4</sup>, D. A. Kirilenko<sup>5,6</sup>, I. A. Rodionov<sup>7</sup>

<sup>1</sup>Institute of Macromolecular Compounds RAS, Bolshoy pr. 31, 199004 St. Petersburg, Russia

<sup>2</sup>Saint Petersburg Electrotechnical University “LETI”, ul. Professora Popova 5, 197376 St. Petersburg, Russia

<sup>3</sup>Peter the Great St. Petersburg Polytechnic University, Polytechnicheskaya ul. 29, 195251 St. Petersburg, Russia

<sup>4</sup>Grebenshchikov Institute of Silicate Chemistry RAS, Makarova nab. 2., letter B, 199034 St. Petersburg, Russia

<sup>5</sup>Ioffe Institute RAS, Politekhnicheskaya ul. 26, 194021 St. Petersburg, Russia

<sup>6</sup>ITMO University, Kronverskii avenue 49, 197101 St. Petersburg, Russia

<sup>7</sup>Institute of Chemistry, Saint Petersburg State University,

Universitetskii prospect 26, Petergof, 198504 St. Petersburg, Russia

alexander.n.bugrov@gmail.com, urs1968@gmail.com, tamarakhamova@gmail.com,

demid.kirilenko@mail.ioffe.ru, i.rodionov@spbu.ru

PACS 78.67. n; 78.67.Bf

DOI 10.17586/2220-8054-2019-10-6-654-665

$\text{Eu}^{3+}$ -doped  $\text{ZrO}_2$  nanostructures in the form of rods, stars, and hollow spheres were prepared by varying hydrothermal conditions. X-ray diffraction, transmission electron microscopy, ultraviolet-visible diffuse reflection spectroscopy, a low-temperature nitrogen adsorption method, Raman spectroscopy and photoluminescence spectra were used to characterize the polymorph modification, surface and optical properties of the  $\text{Zr}_{0.98}\text{Eu}_{0.02}\text{O}_2$  nanophosphors. The  $\text{Eu}^{3+}$  content in a zirconia monoclinic lattice, remained constant for all types of obtained nanostructures in order to reveal the morphology influence on the efficiency of electronic excitation energy transfer from the host matrix to photoactive centers. The decrease of the average size of the coherent scattering regions in the series rods  $\rightarrow$  stars  $\rightarrow$  hollow spheres, is associated with increasing the specific surface area values. At that, in the photoluminescence spectrum, the splitting of the sublevels associated with the monoclinic lattice  $^5\text{D}_0 \rightarrow ^7\text{F}_1$  disappears.

**Keywords:** hydrothermal synthesis, monoclinic zirconia, europium, solid solution, rods, stars, hollow spheres, nanocrystals, energy gap, photoluminescence, lifetime.

Received: 17 June 2019

### 1. Introduction

Currently, metal-oxide semiconductors doped with lanthanide ions (Ln) are widely used in solid-state lighting technologies in the manufacture of LEDs, lasers, field emission and vacuum fluorescence displays, as well as in the medical field for the visualization of drug delivery systems and monitoring changes in implant structure [1–3].

The introduction of trivalent lanthanide ions into the crystal structure of semiconductor oxide leads to weakening of the selection rules for radiative transitions, which is accompanied by splitting of the 4f energy levels [4, 5]. In this case, the prohibition of intra-configuration transitions is weakened for  $\text{Ln}^{3+}$ , since such transitions can be partially resolved by vibronic interaction or by mixing higher configurations into 4f wave functions due to the crystal field effect. However, the luminescence lifetime is usually quite large compared to radiative recombination from other types of excited states [6, 7]. Such phosphors are characterized by narrow emission lines, high color purity, large anti-Stokes shifts, an acceptable quantum yield, and a significant luminescence lifetime [8–10]. Such signs are determined by the efficiency of electron excitation energy transfer from the host matrix to photoactive centers, which is determined by the band gap, the type of crystal structure, the size and morphology of the metal-oxide semiconductor particles, and also the local environment of  $\text{Ln}^{3+}$  ions in the lattice [11, 12]. For instance, the trivalent europium ion ( $\text{Eu}^{3+}$ ) can be used as a spectroscopic probe for site symmetry determination [13].

Among p-type semiconductors, zirconia is the optimal optical medium for lanthanide ions, since it has photochemical stability, a high refractive index, a large band gap, transparency in the visible and near infrared regions of the spectrum, and low phonon energy, which helps to reduce the probability of nonradiative transitions due to multiphonon relaxation [14–16]. In turn, europium (III) ions possess intense luminescence in the red region of the visible spectrum and have an advantage over other lanthanides with an even number of 4f electrons, since their initial transition levels in both the absorption spectrum and the luminescence spectrum are non-degenerate ( $J = 0$ ), which makes absorption and luminescence spectra interpretation easy. In addition, the contribution to the integrated luminescence intensity of the hypersensitive  $^5\text{D}_0 \rightarrow ^7\text{F}_2$  transition can be used to determine whether  $\text{Eu}^{3+}$  is located in the centers of symmetry of the crystal matrix [6].

Precipitation methods [17], combustion [18], sol-gel technology [19], template synthesis [20], hydrothermal treatment [21], aerosol pyrolysis [22], anodizing [23] and impregnation [24] are used to obtain nanostructures of various morphology based on  $\text{ZrO}_2$  doped with europium (III) ions. Among the above synthetic approaches, the hydrothermal method is the most universal, since it allows one to obtain nanomaterials with a narrow particle size distribution, high crystallinity, controlled by morphology and microstructure. Varying the pH of the hydrothermal medium and introducing various mineralizers or surfactants can limit crystallite growth along certain crystallographic directions, contributing to the formation of nanostructures of different morphology based on monoclinic zirconia [25–27].  $\text{ZrO}_2:\text{Eu}^{3+}$  nanophosphors with a baddeleyite structure, as far as we know, were obtained only in the form of rods under hydrothermal conditions. For example, Chen and colleagues obtained 1D nanostructures based on the  $\text{Zr}_{0.98}\text{Eu}_{0.02}\text{O}_2$  solid solution by hydrothermal treatment a mixture of zirconium and europium hydroxides in the presence of cetyltrimethylammonium bromide [28].

The aim of this work was to synthesize nanostructures with different morphology based on monoclinic zirconia doped with  $\text{Eu}^{3+}$  by varying the hydrothermal treatment conditions. After that, it was necessary to study the influence of size, structural and surface characteristics of the obtained nanostructures (rods, stars, hollow spheres) on their optical and photoluminescent properties (excitation and emission spectrum profile, luminescence lifetime).

## 2. Experimental part

In this work, we synthesized nanorods, nanostars and hollow spheres of the  $\text{ZrO}_2$ –2 mol.%  $\text{EuO}_{1.5}$  composition, which are represented by the monoclinic zirconia phase in order to study the features of their photoluminescence.

To synthesize nanorods, 2.54 g of  $\text{ZrOCl}_2 \cdot 8\text{H}_2\text{O}$  and 0.06 g of  $\text{EuCl}_3 \cdot 6\text{H}_2\text{O}$  were dissolved in 15 ml of distilled water, after that a mixture of hydroxides of the corresponding metals was precipitated with continuous stirring, dropwise adding 5 M NaOH solution. The obtained precipitate was dehydrated under hydrothermal conditions at 240 °C and 15 MPa for 24 hours.

Four-pointed nanostars of a given composition were also formed from solutions of zirconium and europium chlorides in a hydrothermal medium under the conditions presented in [29].

In the case of hollow spheres, 1.22 g of zirconyl chloride and 0.03 g of europium (III) chloride were dissolved in 60 ml of a mixture of ethanol-hydrochloric acid, taken in a ratio of 3 to 2. Then, 0.75 g urea was added to the solution, and after its dissolution, all components were transferred to an autoclave. Subsequent hydrothermal treatment was carried out at a temperature of 160 °C, a pressure of 15 MPa and an isothermal exposure time of 24 hours.

At the end of hydrothermal synthesis, all the obtained suspensions of the above-described nanostructures were repeatedly washed with ethanol by centrifugation (8000 rpm) and dried in air to constant weight at 80 °C.

The elemental compositions of synthesized nanostructures were determined using a VEGA 3 SBH scanning electron microscope manufactured by Tescan (Czech Republic) with the Oxford Instruments AZtecOne Go X-ray energy dispersive microanalysis system.

X-ray diffraction (XRD) analysis of  $\text{Eu}^{3+}$ -doped  $\text{ZrO}_2$  nanorods, nanostars and hollow spheres was performed using a Rigaku SmartLab diffractometer (Cu  $K\alpha$  radiation, Tokyo, Japan). The XRD patterns were recorded at a tube voltage of 40 kV, tube current of 40 mA, applying a scan rate of 0.5 °/min in a range of  $2\theta$  angles from 10 to 90°. The determination of zirconia crystalline phases was carried out in Crystallographica Search-Match software by comparing our experimental data with powder diffraction files from the ASTM database. The average size of the coherent scattering regions was calculated from XRD line broadening of  $\text{ZrO}_2$ –2 mol.%  $\text{EuO}_{1.5}$  nanostructures in the PD-Win 4.0 program complex using the Scherrer equation.

The size, shape and phase composition of the  $\text{ZrO}_2:\text{Eu}^{3+}$  nanoaggregates and crystallites forming them were established using a JEM-2100F transmission electron microscope manufactured by JEOL (Tokyo, Japan) at an acceleration voltage of 90 kV.

The specific surface area of powders of the  $\text{ZrO}_2$ –2 mol.%  $\text{EuO}_{1.5}$  composition in the form of rods, four-pointed stars and hollow spheres was measured by the low-temperature nitrogen adsorption method using a QuantaChrome Nova 4200V analyzer. Samples were degassed at 150 °C under vacuum for 16 hours before measurement. The specific surface area ( $S_{BET}$ ) of samples was calculated based on the experimental data using the models: Brunauer–Emmett–Teller (BET) at 7 points in the range of partial pressures of nitrogen  $P/P_0 = 0.07 \div 0.25$  and Langmuir. The pore size distribution was calculated based on nitrogen adsorption–desorption isotherms according to the Barrett–Joyner–Halenda (BJH) method.

Raman spectra were recorded in the backscattering geometry using a Jobin Yvon T64000 triple monochromator equipped with a liquid  $\text{N}_2$ -cooled charge-coupled device detector. The excitation wavelength  $\lambda$  was 488 nm from an  $\text{Ar}^+$  laser with a typical laser power of  $\sim 1$  mW.

The photoluminescence emission spectra were recorded using a Horiba LabRAM HR Evolution system equipped with a He–Cd excitation laser emitting at 325 nm with a maximum power of 1 mW. Photoluminescence decay and excitation spectra were measured using the luminescence spectrophotometer LS-100 (PTIR®, Canada).

The optical absorption edge energy of nanostructures based on zirconia was determined using diffuse reflectance spectra (Shimadzu UV-2550 spectrophotometer equipped with an ISR-2200 integrating sphere) by the standard procedure from the cross point of linear sections of the Schuster–Kubelka–Munk function plot in the coordinates  $(F(R) \times h\nu)^{1/2} = f(h\nu)$ .

### 3. Results and discussion

The different morphology nanostructures based on  $\text{ZrO}_2$  prepared in this study contained 2 at.%  $\text{Eu}^{3+}$  according to energy dispersive X-ray (EDX) spectroscopy (Table 1).

TABLE 1. EDX-analysis data of  $\text{Eu}^{3+}$ -doped  $\text{ZrO}_2$  nanostructures with different morphology

| Morphology     | Zr     | Eu  | Hf  | Na  | Cl  |
|----------------|--------|-----|-----|-----|-----|
|                | at., % |     |     |     |     |
| Nanorods       | 96.8   | 2.1 | 0.6 | 0.5 | —   |
| Nanostars      | 96.7   | 2.0 | 0.6 | 0.7 | —   |
| Hollow spheres | 96.1   | 2.1 | 0.8 | —   | 1.0 |
|                | wt., % |     |     |     |     |
| Nanorods       | 95.3   | 3.4 | 1.2 | 0.1 | —   |
| Nanostars      | 95.4   | 3.2 | 1.2 | 0.2 | —   |
| Hollow spheres | 94.6   | 3.5 | 1.5 | —   | 0.4 |

Phosphors in the form of nanorods were formed in a strongly alkaline medium under hydrothermal treatment of a  $\text{ZrO}(\text{OH})_2\text{--Eu}(\text{OH})_3$  mixture precipitated from solutions of their chlorides. Qualitative phase analysis based on XRD of the  $\text{ZrO}_2\text{--}2 \text{ mol.}\% \text{EuO}_{1.5}$  one-dimensional nanostructures using the PDWin 4.0 and Crystallographica Search-Match software packages showed their greatest correspondence to the baddeleyite structure (Card No. 24-1165 according to the ASTM database [30], Fig. 1, pattern 1). The average size of coherent scattering regions calculated by the Scherrer equation was  $30 \pm 5$  nm. The length of the nanorods was about 150 nm, and the width was 50 nm, according to TEM micrographs (Fig. 2a, line 1). In addition to twin reflections of monoclinic (*m*)  $\text{ZrO}_2\text{--}2 \text{ mol.}\% \text{EuO}_{1.5}$  rods elongated along the (100) plane, concentric rings indicating the presence of small crystallites with a tetragonal (*t*) structure were also observed in the electron microdiffraction image (Fig. 2b, line 1). Apparently, initially formed under hydrothermal conditions  $\text{Eu}^{3+}$ -stabilized *t*- $\text{ZrO}_2$  nanocrystals with an average size of  $\sim 5 \pm 1$  nm (Fig. 3) gradually dissolve at high pH medium values and recrystallize along the crystallographic direction (100) with the formation of monoclinic rice-like structures.

Hydrothermal synthesis of  $\text{ZrO}_2\text{--}2 \text{ mol.}\% \text{EuO}_{1.5}$  nanostars from the same precursors was carried out in the presence of sodium acetate. Its  $\text{CH}_3\text{COO}^-$  ions adsorbed on the surface of the germinal centers promoted the subsequent crystallization of zirconia along the direction perpendicular to the (101) planes. The resulting structures with a size of about 100 nm (Fig. 2a, line 2) have the shape of four-pointed stars with numerous outgrowth 7 nm wide according to TEM data. An electron diffraction pattern shows the presence of *m*- $\text{ZrO}_2$  with multiple twinning along the (100) plane (Fig. 2b, line 2). The observed diffraction maxima in the XRD pattern of  $\text{ZrO}_2\text{--}2 \text{ mol.}\% \text{EuO}_{1.5}$  nanostars also refer exclusively to the monoclinic phase of zirconia, and the average size of the coherent scattering regions (CSR) for this sample is  $12 \pm 2$  nm according to calculations (Fig. 1, pattern 2).

High-temperature hydrolysis of zirconyl and europium chlorides in the presence of urea produced nanostructures in the form of hollow microspheres (Fig. 2a, line 3) using a mixture of ethanol and hydrochloric acid in a ratio of 3:2 as a hydrothermal medium. In this case, the formation of the observed structures under hydrothermal conditions occurs by the mechanism of emulsion template synthesis. Ethanol in the presence of concentrated hydrochloric acid dehydrates with increasing temperature to form diethyl ether, which, due to its low solubility in water, can exist as droplets of oil in this solution [31]. The urea present in the initial mixture slowly reacts with water, forming  $\text{NH}_4\text{OH}$

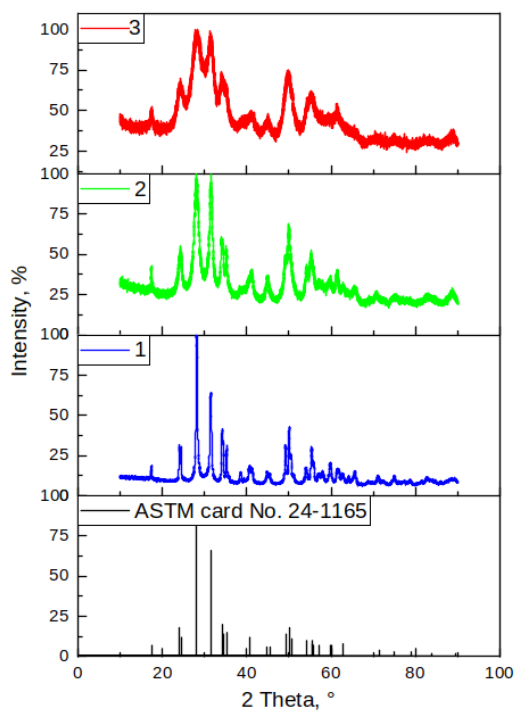


FIG. 1. XRD patterns of  $ZrO_2$ -2 mol.%  $EuO_{1.5}$  nanostructures in the form of nanorods (1), nanostars (2) and hollow spheres (3)

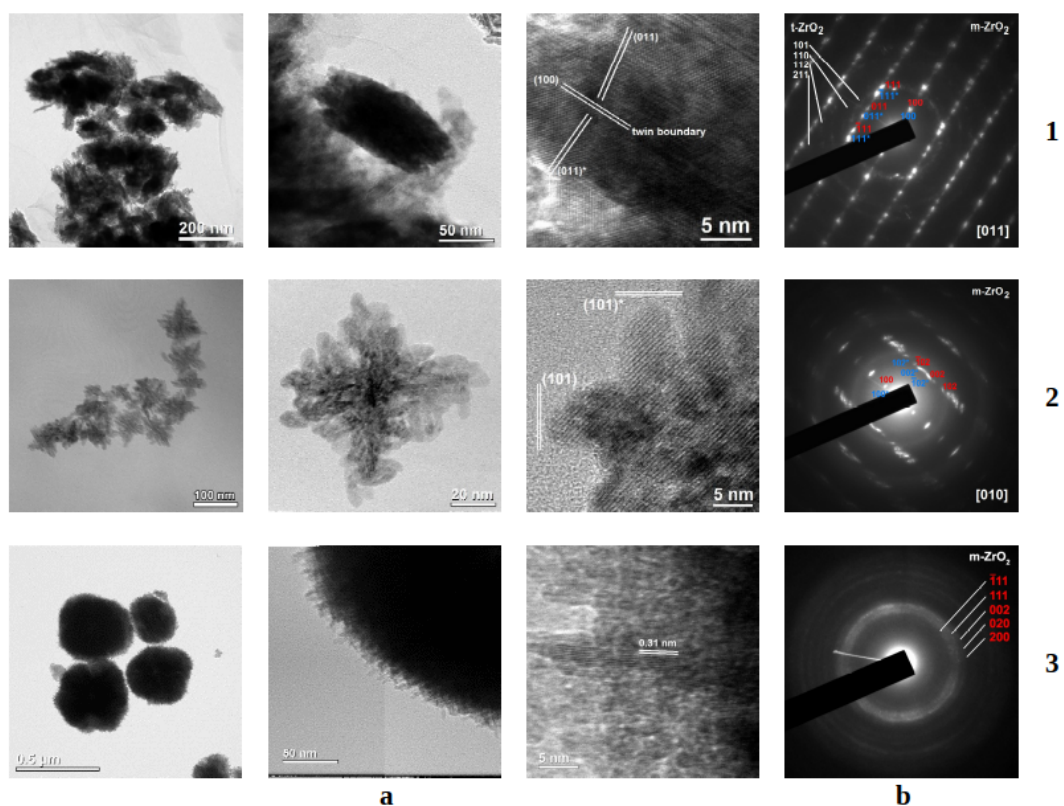


FIG. 2. TEM micrographs (a) and electron microdiffraction patterns (b) of  $ZrO_2$ -2 mol.%  $EuO_{1.5}$  nanostructures in the form of nanorods (1), nanostars (2) and hollow spheres (3)

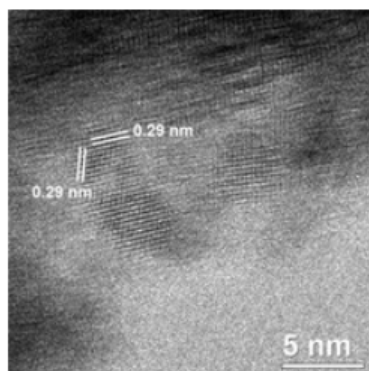


FIG. 3. TEM micrographs of quasispherical tetragonal zirconia nanoparticles of which rice-like  $\text{ZrO}_2$ -2 mol.%  $\text{EuO}_{1.5}$  structures subsequently form under hydrothermal conditions

and  $\text{CO}_2$ , which leads to an increase in pH and, as a result, hydrolysis of  $\text{ZrOCl}_2$  and  $\text{EuCl}_3$  at the “oil drop – solution” interface. A shell of  $\text{ZrO}_2$ -2 mol.%  $\text{EuO}_{1.5}$  crystallites is formed on the surface of ether drops in the process of hydroxide dehydration and subsequent isothermal exposure. In accordance with the powder XRD data, the hollow inorganic structures obtained in this way are an assembly of monoclinic zirconia crystallites with an average size of  $5 \pm 1$  nm (Fig. 1, pattern 3). TEM images of microspheres show nanowires with a diameter of about 5 nm, assembled into spherical aggregates of submicron size ( $\sim 400$  nm, Fig. 2a, line 3). The structure of the aggregates corresponds to the monoclinic phase of zirconia (Fig. 2b, line 3).

According to the results of low-temperature nitrogen adsorption, nanocrystalline  $\text{ZrO}_2$ -2 mol.%  $\text{EuO}_{1.5}$  powders of rods, stars, and hollow spheres are characterized by the specific surface area of 19.1, 92.3 and 151.1  $\text{m}^2/\text{g}$ , respectively (Table 2). At the same time, the BET constant values for samples of nanoparticles collected in the form of rods and hollow spheres are equal to 508 and 745, respectively. This fact is indicative of the presence of a significant amount of micropores in these powders. Based on the foregoing, the assessment of the specific surface area for  $\text{ZrO}_2$ -2 mol.%  $\text{EuO}_{1.5}$  powders with different morphology nanostructures was also carried out using the Langmuir model operating in the limit of monomolecular adsorption, i.e. adsorption on the surface of micropores (Table 2).

TABLE 2. The structure parameters determined using low-temperature nitrogen adsorption for powders consisting of  $\text{ZrO}_2$ -2 mol.%  $\text{EuO}_{1.5}$  nanoaggregates with different morphology

| Morphology     | $S_{BET}$ , $\text{m}^2/\text{g}$ | $S_{Langmuir}$ , $\text{m}^2/\text{g}$ | $D_1$ , nm | $D_2$ , nm | $V_{pore}^*$ , $\text{cm}^3/\text{g}$ |
|----------------|-----------------------------------|--|------------|------------|---------------------------------------|
| Nanorods       | $19.1 \pm 0.2$                    | 32                                     | 2.6        | 42.2       | 0.35                                  |
| Nanostars      | $92.3 \pm 1.8$                    | —                                      | 2.2        | 13.4       | 0.22                                  |
| Hollow spheres | $151.1 \pm 1.5$                   | 223.9                                  | —          | —          | 0.14                                  |

\* The specific pore volume is determined by the maximum filling ( $P/P_0 = 0.99$ ).

According to Fig. 4, the full adsorption-desorption isotherms for these powders substantially depend on their morphology. For example, the full isotherm for a powder consisting of  $\text{ZrO}_2$ -2 mol.%  $\text{EuO}_{1.5}$  nanorods is close to type II, which is inherent in non-porous and macroporous samples. At the same time, the weak hysteresis and a high BET constant indicate the presence of a certain amount of micro and mesopores in this sample. This hysteresis can be classified as type H1 according to IUPAC, when the material has cylindrical pores open on both sides. Thus, the full isotherm can be attributed to the combined type (Fig. 4, isotherm 1).

The full isotherm of powder consisting of  $\text{ZrO}_2$ -2 mol.%  $\text{EuO}_{1.5}$  nanostars clearly belongs to type IV, which is typical for mesoporous materials. Adsorption and capillary condensation can occur in the pores of such materials, which leads to the appearance of hysteresis between the adsorption-desorption isotherms (Fig. 4, isotherm 2). The course of the capillary-condensation hysteresis loop for a given nanopowder according to the IUPAC can be classified as type H2, which indicates the presence of bottle-shaped mesopores in it.

Finally, the full isotherm for a powder consisting of  $\text{ZrO}_2$ -2 mol.%  $\text{EuO}_{1.5}$  hollow spheres is close to type I, which is mainly fixed in microporous samples (Fig. 4, isotherm 3). Moreover, the presence of a weakly expressed loop of capillary-condensation hysteresis on the full isotherm confirms the presence of a certain amount of mesopores

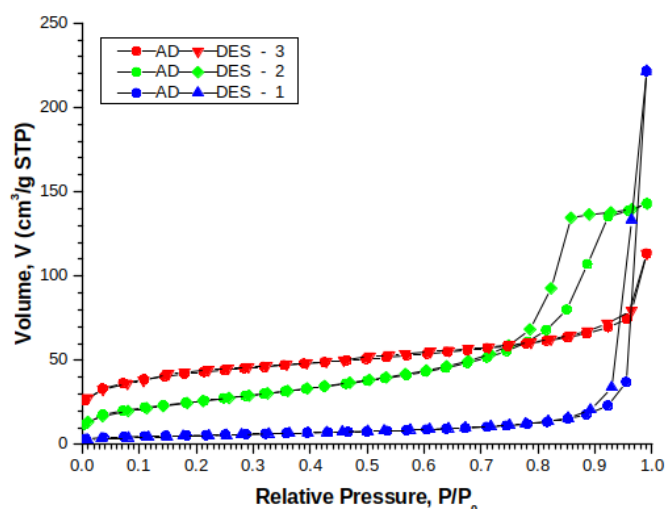


FIG. 4. Adsorption-desorption isotherms of powders consisting of  $\text{ZrO}_2$ -2 mol.%  $\text{EuO}_{1.5}$  nanostructures with different morphology: rods (1), stars (2), hollow spheres (3)

in this sample. This type is the H4 hysteresis according to the IUPAC classification, which is characteristic of pore slit-like form.

Pore size distributions calculated for the desorption branch according to the BJH algorithm for powders consisting of  $\text{ZrO}_2$ -2 mol.%  $\text{EuO}_{1.5}$  nanostructures with different morphology are shown in Fig. 5. Obviously, the porosity of these nanopowders substantially depends on morphology. A bimodal pore size distribution with maxima in the micro  $D_1$  and mesopore  $D_2$  regions is characteristic of powders containing nanostructures in the form of stars and rods (Table 2), respectively. In the case of the sample consisting of  $\text{ZrO}_2$ -2 mol.%  $\text{EuO}_{1.5}$  hollow spheres, a uniformly decreasing pore size distribution in the range from 1.5 to 40 nm is observed, which confirms the presence of both micro- and mesopores in it.

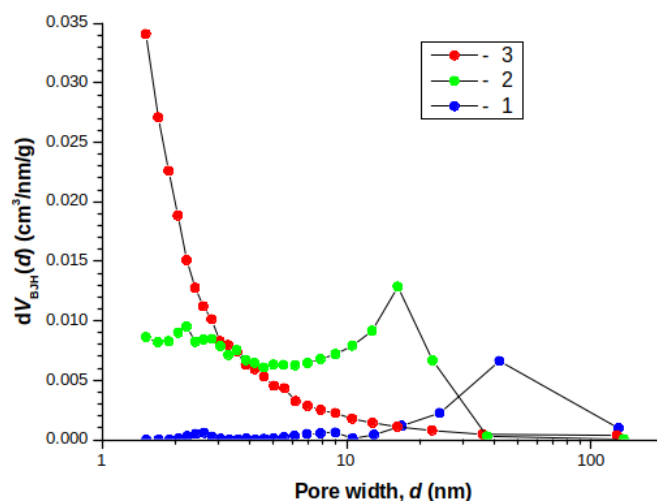


FIG. 5. Pore size distributions calculated according to the BJH algorithm for powders consisting of  $\text{ZrO}_2$ -2 mol.%  $\text{EuO}_{1.5}$  nanostructures with different morphology: rods (1), stars (2), hollow spheres (3)

An intense peak at 614 nm is observed in the luminescence spectra of  $\text{ZrO}_2$ -2 mol.%  $\text{EuO}_{1.5}$  nanostructures with different morphology and there is no component of the electric dipole transition in the region of 606 nm. This indicates the absence of cubic and tetragonal polymorphic modifications and localization of  $\text{Eu}^{3+}$  in the less symmetrical environment of the  $m$ - $\text{ZrO}_2$  for the synthesized phosphors (Fig. 6a). With an increase in the resolution of the luminescent equipment, one can see narrow peaks of fine splitting upon excitation at 325 nm not only in the spectral term  ${}^7F_2$ ,

but also in  ${}^7F_4$  for  $\text{Eu}^{3+}$ . Such a splitting pattern allows us to conclude that the monoclinic phase is exceptionally prevalent for nanorods. At the same time, for nanostars and hollow spheres, the order of the monoclinic phase is disrupted due to internal stresses and a decrease in the size of crystallites. A similar violation of the long-range order also manifests itself in Raman spectra (Fig. 7) in the form of the contribution of the diffuse band in the range  $400 - 700 \text{ cm}^{-1}$ . Because of this, the fine splitting between 614 and 625 nm disappears in the luminescence spectra, which leads to an increase in the contribution to the luminescence band at 616 nm, as well as to the disappearance of the peak at 711 nm and a predominance of the contribution at 700 nm (compare spectrum 1 with spectra 2 and 3 in Fig. 6a).

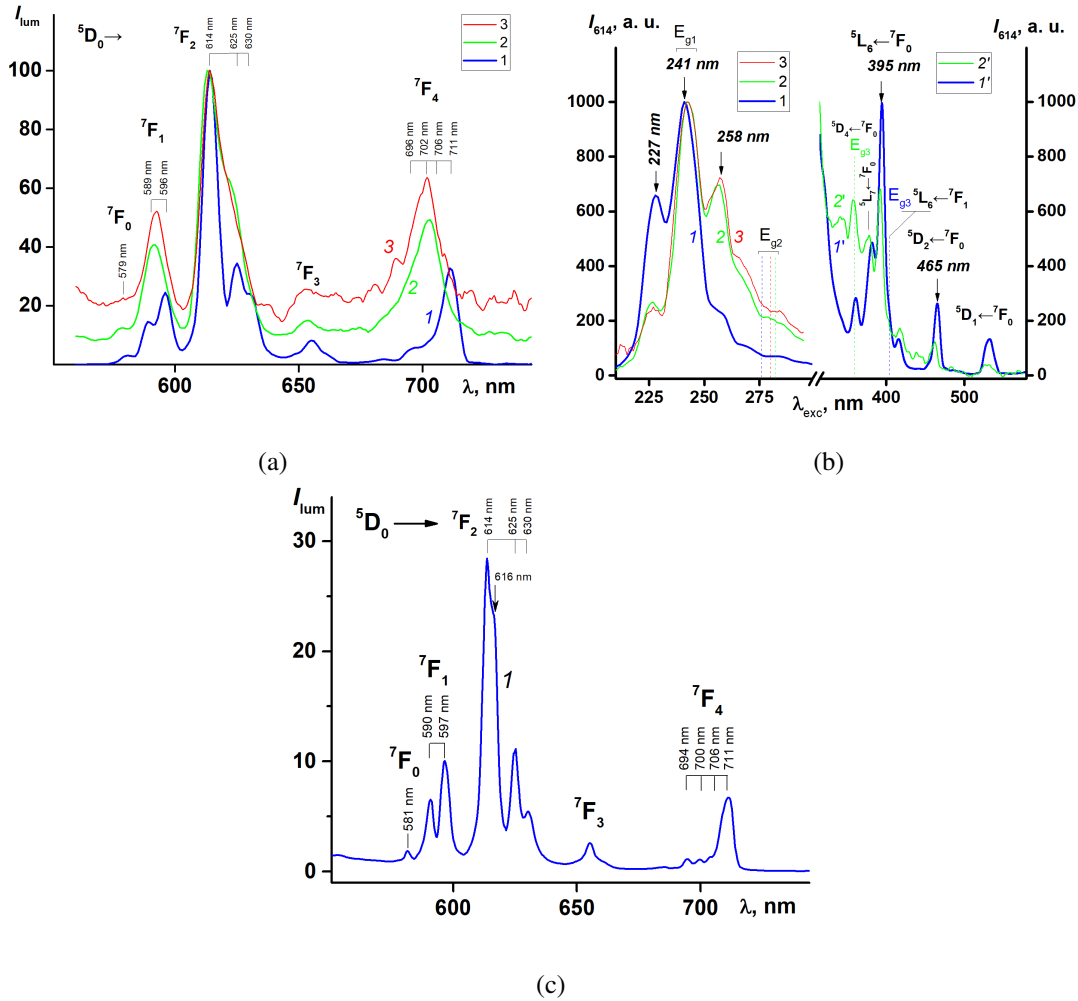


FIG. 6. Emission spectra (a, c) and excitation spectra (b) of luminescence for nanorods (1, 1'), nanostars (2, 2'), and hollow spheres (3) of the  $\text{ZrO}_2-2 \text{ mol.}\% \text{EuO}_{1.5}$ , normalized at 614 and 241 nm, respectively. Excitation 242 (a) and 325 nm (c)

The luminescence excitation spectra of europium (III) ions in the structure of zirconia nanostars and hollow spheres are identical (Fig. 6b, spectra 2 and 3). In the case of nanorods, a more efficient absorption of electronic excitation energy is recorded in the region of hard ultraviolet, especially at wavelengths of 227 and 241 nm (Fig. 6b, spectrum 1). This excitation band with a maximum peak at 241 nm and several additional local extrema at 227 and 258 nm corresponds to the  $\text{O}^{2-}-\text{Eu}^{3+}$  charge transfer resulting from electron transitions from the 2p orbital of  $\text{O}^{2-}$  to the 4f orbital of  $\text{Eu}^{3+}$ .

In the Raman spectrum for  $\text{ZrO}_2-2 \text{ mol.}\% \text{EuO}_{1.5}$  nanorods, the characteristic peaks correspond to the monoclinic crystal lattice at 178, 189, 305, 380, 474, 537, 556, 612 and  $631 \text{ cm}^{-1}$  (Fig. 7, spectrum 1). For nanostars and hollow spheres in the Raman spectra region of  $400 - 700 \text{ cm}^{-1}$ , a diffuse scattering band is detected, which is associated with the disappearance of long-range order due to internal stresses and twinning. A similar effect of the disappearance of the long-range order of the monoclinic phase was also found in the luminescence spectra (see Fig. 6 and in the text above).

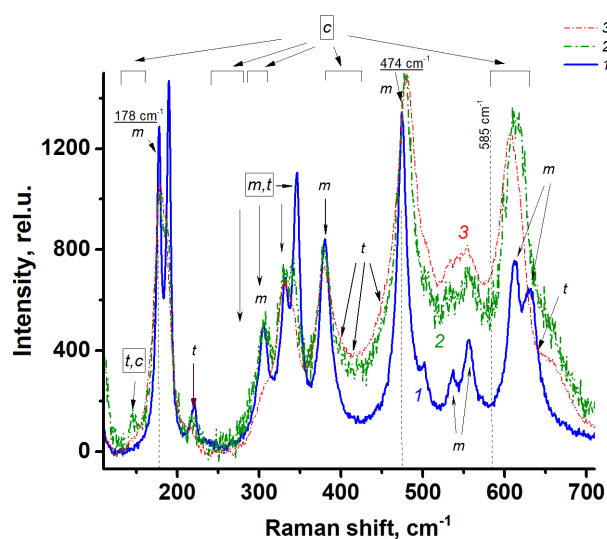


FIG. 7. Raman spectra for nanorods (1), nanostars (2) and hollow spheres (3) of  $\text{ZrO}_2$ -2 mol.%  $\text{EuO}_{1.5}$ , normalized at  $474 \text{ cm}^{-1}$

Based on the diffuse reflectance spectra  $R(\lambda)$  in the visible and ultraviolet range from 1.5 to 6 eV, one calculated the Schuster–Kubelka–Munk (SKM) or remission function [32]:

$$F(R_\infty(\lambda)) = \frac{(1 - R_\infty(\lambda))^2}{2R_\infty(\lambda)} = \frac{K}{S} = \frac{2.303\varepsilon C}{S}, \quad (1)$$

where  $K$  is the absorption coefficient (twice the Beer's law absorption coefficient);  $S$  is twice the scattering coefficient of the sample;  $\varepsilon$  is the absorptivity, and  $C$  is the analyte concentration.

Using the Tauc plot of  $(F(R_\infty)h\nu)^{1/\eta}$  versus energy,  $h\nu$ , one estimated the energy gap,  $E_g$ , between the conduction band and the valence one in  $\text{Zr}_{0.98}\text{Eu}_{0.02}\text{O}_{1.99}$  nanoparticles (Fig. 8).

In the region of the energy obtained from 2 to 6 eV, the indirect allowed absorption transitions turned out to manifest themselves because there are linear approximations at  $\eta = 2$  for all the cases under investigation [33]. At that, the  $E_g$  values of the studied nanostructures are found from 3.07 to 5.13 eV (Table 3), which is consistent with work [34]. Analysis of the Tauc spectra showed that the widest absorption edge energy ( $E_{g1}$ ) of ca. 5.1 eV clearly manifests itself for all the studied zirconia nanostructures containing  $\text{Eu}^{3+}$  [35]. There is no dependence of  $E_{g1}$  on the morphology of the nanoparticles. The absorption connected with it corresponds in the luminescence excitation spectra to a maximum of 241 nm (compare Fig. 6b and Table 3).

TABLE 3. Energy gap parameters as obtained from Tauc plots for  $\text{Zr}_{0.98}\text{Eu}_{0.02}\text{O}_{1.99}$  nanoparticles with a different morphology

| Morphology     | Coherent scattering region, nm | Energy gap parameters, eV (wavelength, nm) <sup>1)</sup> |                     |                     |
|----------------|--------------------------------|--|---------------------|---------------------|
|                |                                | $E_{g1}(\lambda_1)$                                      | $E_{g2}(\lambda_2)$ | $E_{g3}(\lambda_3)$ |
| Nanorods       | $30 \pm 5$                     | 5.10 (243)   | 4.49 (276)          | 3.07 (404)          |
| Nanostars      | $12 \pm 2$                     | 5.11 (243)   | 4.39 (282)          | 3.42 (362)          |
| Hollow spheres | $5 \pm 1$                      | 5.13 (242)   | 4.42 (280)          | 3.57 (347)          |

<sup>1)</sup> One uses the relationship between energy in eV and the corresponding wavelength in nm as  $E \cdot \lambda = 1240 \text{ eV}\cdot\text{nm}$ .

The presence in the band of the PL excitation spectrum for all synthesized nanostructural forms of maxima at 227 and 240 – 243 nm, as well as the  $E_{g1}$  values of 5.10 – 5.13 eV indicate the existence of inter-configuration transitions in  $m\text{-ZrO}_2$  [36]. Besides, the largest contribution occurs at 258 nm for nanostars and hollow spheres

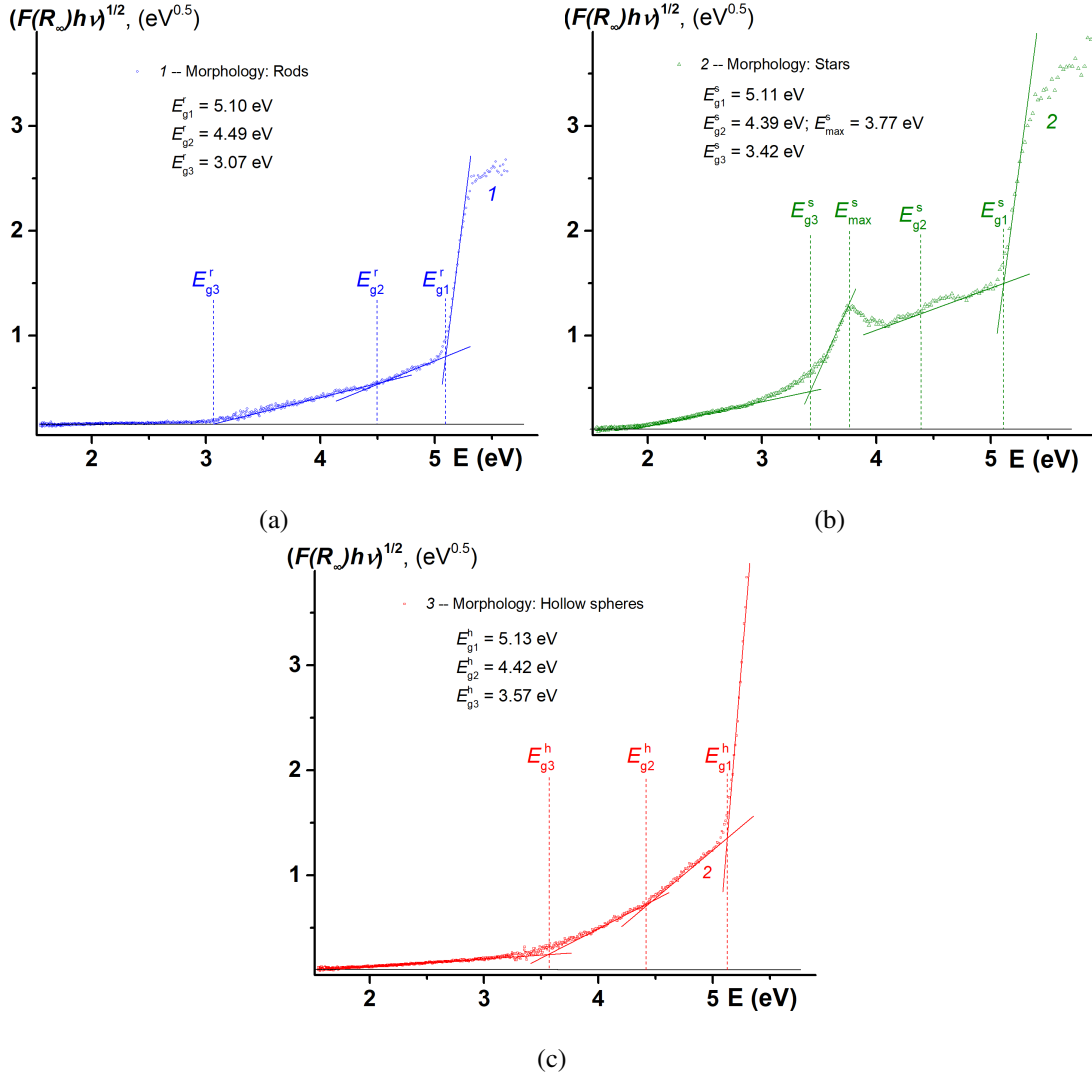


FIG. 8. Tauc plot spectra for nanorods (a), nanostars (b) and hollow nanospheres (c) of  $ZrO_2-2 \text{ mol.}\% \text{ EuO}_{1.5}$

(compare normalized excitation spectra in Fig. 6b), which designates charge transfer ( $\text{Eu}^{3+} \leftarrow \text{O}^{2-}$ ) for the type of  $Zr-O$  bond of  $2.1297 \text{ \AA}$  in a monoclinic cell [35]. This indicates a perfect (with a large CSR) monoclinic phase in this case and is confirmed by other methods (XRD and RS). A change in the monoclinic modification and a decrease in its CSR (Table 3) is indicated by a shift in the excitation spectra from 241 to 243 nm during the transition to nanostars and hollow spheres. In addition, a diffuse band appears in the Raman spectra and the clear splitting of the monoclinic phase at  $178 \text{ cm}^{-1}$  disappears. As seen above, one can assume the formation of t,c-phase crystallites with a small CSR. The manifestation of the value of  $E_{\text{max}}$  3.77 eV (Fig. 8b) for nanostars may indicate a low coordination of the bond with the  $t\text{-}ZrO_2$  surface ( $Zr^{4+} \leftarrow O^{2-}$ ) [36].

The decay of PL intensity ( $I_{lum}(t)$ ) for nanoparticles can be approximated by a model of the dual exponential function:

$$I_{lum}(t) = A_1 \cdot \exp(-t/\tau_{PL1}) + A_2 \cdot \exp(-t/\tau_{PL2}) + B, \quad (2)$$

where  $\tau_{PL1}$  and  $\tau_{PL2}$  are the PL lifetime for the first and second emission processes;  $A_1$  and  $A_2$  are the first and second pre-exponential factors. Term  $B$  is a background contribution. Based on the obtained  $\tau_{PL}$  and their contributions in the two-exponential approximation (Table 4), the weighted-average luminescence lifetimes,  $\tau_{PLw}$ , are calculated according to the equation:

$$\tau_{PLw} = \frac{\sum_{i=1}^2 A_i \tau_{PLi}^2}{\sum_{i=1}^2 A_i \tau_{PLi}}. \quad (3)$$

TABLE 4. Photoluminescence lifetimes<sup>1)</sup> of  $Zr_{0.98}Eu_{0.02}O_{1.99}$  nanoparticles of a different morphology

| Morphology     | $A_1$    | $\tau_{PL1}$ , ms | $A_2 = 1 - A_1$ | $\tau_{PL2}$ , ms | $\chi^2$ | $\tau_{PLw}$ , ms <sup>2)</sup> | $DWP$ <sup>3)</sup> |
|----------------|----------|-------------------|-----------------|-------------------|----------|---------------------------------|---------------------|
| Nanorods       | 0.452(7) | 0.455(8)          | 0.548(8)        | 1.31(1)           | 2.147    | 1.120                           | 0.518               |
| Nanostars      | 0.85(2)  | 0.248(7)          | 0.15(1)         | 0.69(6)           | 0.610    | 0.394                           | 1.577               |
| Hollow spheres | 0.71(6)  | 0.064(9)          | 0.29(2)         | 0.49(3)           | 1.05     | 0.387                           | 1.769               |

<sup>1)</sup> PL lifetimes were fitted on the basis of the dual exponent decay (see Eq. 2) in minimizing a reduced  $\chi^2$ -statistics.

<sup>2)</sup> Note the mean-weighted PL lifetimes,  $\tau_{PLw}$ , calculated upon Eq. 3.

<sup>3)</sup> Darbin–Watson statistic parameter [37].

According to the data shown in Table 4, in a two-exponential approach both PL lifetimes  $\tau_{PL1}$  and  $\tau_{PL2}$  increase depending on morphology in series: hollow spheres to nanorods. Moreover, for the morphology of nanorods in the Raman spectra, a characteristic splitting of peaks corresponding to the monoclinic structure at 178 and 189  $\text{cm}^{-1}$  is observed (Fig. 7). In the photoluminescence spectra for nanorods with  $\text{Eu}^{3+}$ , a fine splitting characteristic of  $m\text{-ZrO}_2$  is observed in the spectral terms  ${}^7F_2$  at 614, 625, 630 nm and  ${}^7F_4$  at 694, 700, 706 and 711 nm (Fig. 6c). In these spectral terms, a characteristic intensity distribution pattern is observed with a maximum contribution at 614 nm in  ${}^7F_2$  and 711 nm in  ${}^7F_4$ . The contributions to  ${}^7F_4$  at 694, 700, and 706 nm are insignificant. In the  ${}^7F_2$  term, the maximum of 614 nm has a shoulder at 616 nm. In nanorods, the formation of crystallites with a well-formed long-range order of the monoclinic phase (CSR ca. 30 nm) is also indicated by the manifestation of the  ${}^5D_0 \rightarrow {}^7F_0$  optical transition in the luminescence spectrum. In addition, in this system, the  ${}^5D_0 \rightarrow {}^7F_1$  magnetic dipole transition is characterized by splitting into two peaks at 590 and 597 nm. For nanostars, the optical transition  ${}^5D_0 \rightarrow {}^7F_0$  manifests itself less, and for hollow spheres it practically disappears (Fig. 6a). For nanostars and hollow spheres in the optical term  ${}^7F_1$ , which is responsible for the magnetic dipole transition, fine splitting is not observed as for nanorods. The contribution at 625 nm compared to 614 nm grows in the order of nanorods  $\rightarrow$  nanostars  $\rightarrow$  hollow spheres, which leads to a greater “diffuseness” of the photoluminescence spectrum – the absence of pronounced fine splitting in the terms  ${}^7F_1$ ,  ${}^7F_2$  and  ${}^7F_4$ . This fact is consistent with Raman spectra, in which a diffuse scattering band appears during the transition from nanorods to nanostars (compare spectra 1 and 2 in Fig. 7). Moreover, the contribution of the diffuse band increases further during the transition from nanostars to hollow spheres (compare spectra 2 and 3 in Fig. 7). The appearance of a diffuse band in Raman spectra can be explained by CSR reduction in the series of nanorods  $\rightarrow$  nanostars  $\rightarrow$  hollow spheres (Table 3), and hence a decrease in the crystalline order in this series, as well as an increase in the amorphous component because of the growth of nanostructure surface area relating to volume (Table 2). This effect manifests itself if we compare the luminescence lifetimes in this order. The weighted-average luminescence lifetime decreases, indicating that the reduction in symmetry due to an increase in the contribution, which is more pronounced with a smaller CSR size and high  $S_{BET}$  values (Tables 2, 4). Thus, the most ordered monoclinic crystalline structure, in which the long-range order in the crystallite extends to 30 nm, is formed in nanorods. Disturbance of long-range order in nanostars is due to twinning, in hollow spheres – due to the presence of internal strains. The nanostar CSR is two to three times smaller than for nanorods, which is associated with the “splitting” of the crystallite into parts. In hollow spheres, the CSR is the lowest 6 nm, since the geometry of the sphere must have the strongest internal strains.

#### 4. Conclusions

In this study, we examined the structure, morphology and emission properties of  $\text{Eu}^{3+}$ -doped zirconia nanophosphors using X-ray diffraction, Raman, UV-visible diffuse reflectance and photoluminescence spectroscopy. Earlier in [28], monoclinic  $Zr_{0.98}Eu_{0.02}O_2$  nanorods with the lowered local site symmetry for photoactive centers were obtained by surfactant-assisted hydrothermal process. The authors observed the transformation of spherical particles of a tetragonal polymorphic modification with a size of less than 10 nm into lamellar structures of the same phase composition, which turned into  $m\text{-ZrO}_2$  nanorods, as basicity of the hydrothermal medium increases. In turn, we have obtained  $ZrO_2$  nanostructures with a low content of  $\text{Eu}^{3+}$  (2 mol.%) in the form of rods, stars, and hollow spheres from the same precursors with varying hydrothermal conditions. Regardless of morphology, all synthesized nanoobjects are a monoclinic polymorphic modification of zirconia. A less defective structure of monoclinic zirconia was formed as the size of crystallites increased in a series of hollow spheres, stars and rods. Morphology is reflected in

different luminescent properties. The more regular monoclinic structure, the longer luminescence lifetime: rods have 1.12 ms versus  $\sim 0.4$  ms for stars and hollow spheres. A comparison of the Tauc plots for the SKM function and the photoluminescence excitation spectra shows (Zr–O–Eu) charge-transfer states and energy transfer to  $\text{Eu}^{3+}$  in the  $\text{ZrO}_2$  matrix with an absorption edge energy of 4.80 – 5.13 eV. While decreasing the coherent scattering volume, the adsorption surface area in the series rods–stars–hollow spheres increases.

### Acknowledgements

Alexander N. Bugrov appreciates the Russian Foundation for Basic Research (grant No. 16-33-60227) for the financial support.

Ruslan Smyslov is thankful for his funding received from the EU-H2020 research and innovation program under grant agreement No. 654360, having benefitted from the access provided by CEA/LETI in Grenoble within the framework of the NFFA-Europe Transnational Access Activity. X-ray diffraction experiments were performed on the Engineering Center equipment of the St. Petersburg State Technological Institute (Technical University). TEM studies were carried out in the Federal Joint Research Center “Material science and characterization in advanced technology” funded by the Ministry of Education and Science of the Russian Federation (id RFMEFI62117X0018).

### References

- [1] Dhoble S.J., Pawade V.B., Swart H.C., Chopra V. Spectroscopy of lanthanide doped oxide materials. Woodhead Publishing, 2019, 480 p.
- [2] Cesaria M., Di Bartolo B. Nanophosphors-based white light sources. *Nanomaterials*, 2019, **9** (7), 1048.
- [3] Gai S., Li C., Yang P., Lin J. Recent progress in rare earth micro/nanocrystals: Soft chemical synthesis, luminescent properties, and biomedical applications. *Chemical Reviews*, 2014, **114** (4), P. 2343–2389.
- [4] Maciel G.S., Rakov N. Photon conversion in lanthanide-doped powder phosphors: concepts and applications. *RSC Advances*, 2015, **5**, P. 17283–17295.
- [5] Ma C.-G., Brik M.G., et al. Spectroscopic and crystal-field analysis of energy levels of  $\text{Eu}^{3+}$  in  $\text{SnO}_2$  in comparison with  $\text{ZrO}_2$  and  $\text{TiO}_2$ . *Journal of Alloys and Compounds*, 2011, **509**, P. 3441–3451.
- [6] Binnemans K. Interpretation of europium (III) spectra. *Coordination Chemistry Reviews*, 2015, **295**, P. 1–45.
- [7] Nadort A., Zhao J., Goldys E.M. Lanthanide upconversion luminescence at a nanoscale: fundamentals and optical properties. *Nanoscale*, 2016, **8**, P. 13099–13130.
- [8] Debashrita S., Sagar G., Tuhin S., Venkataraman M. Design of lanthanide-doped colloidal nanoparticles: Applications as phosphors, sensors and photocatalysts. *Langmuir*, 2019, **35** (19), P. 6211–6230.
- [9] Bugrov A.N., Smyslov R.Yu., et al. Soluble and insoluble polymer-inorganic systems based on poly(methyl methacrylate), modified with  $\text{ZrO}_2\text{-LnO}_{1.5}$  (Ln = Eu, Tb) nanoparticles: Comparison of their photoluminescence. *Journal of Luminescence*, 2019, **207**, P. 157–168.
- [10] Prakashbabu D., Ramalingam H.B., et al. Charge compensation assisted enhancement of photoluminescence in combustion derived  $\text{Li}^+$  co-doped cubic  $\text{ZrO}_2\text{:Eu}^{3+}$  nanophosphors. *Phys. Chem. Chem. Phys.*, 2016, **18**, P. 29447–29457.
- [11] Soares M.R., Rodrigues J., et al. Prospects on laser processed wide band gap oxides optical materials. *Proceedings of SPIE*, 2013, **8626**, 862607.
- [12] Bugrov A.N., Smyslov R.Yu., et al. Phase composition and photoluminescence correlations in nanocrystalline  $\text{ZrO}_2\text{:Eu}^{3+}$  phosphors synthesized under hydrothermal conditions. *Nanosystems: Physics, Chemistry, Mathematics*, 2018, **9** (3), P. 378–388.
- [13] Tiseanu C., Cojocaru B., et al. Order and disorder effects in nano- $\text{ZrO}_2$  investigated by micro-Raman and spectrally and temporarily resolved photoluminescence. *Phys. Chem. Chem. Phys.*, 2012, **14**, P. 12970–12981.
- [14] Meetei S.D., Singh S.D. Effects of crystal size, structure and quenching on the photoluminescence emission intensity, lifetime and quantum yield of  $\text{ZrO}_2\text{:Eu}^{3+}$  nanocrystals. *Journal of Luminescence*, 2014, **147**, P. 328–335.
- [15] Bugrov A.N., Smyslov R.Yu., Zavialova A.Yu., Kopitsa G.P. The influence of chemical prehistory on the structure, photoluminescent properties, surface and biological characteristics of  $\text{Zr}_{0.98}\text{Eu}_{0.02}\text{O}_{1.99}$  nanophosphors. *Nanosystems: Physics, Chemistry, Mathematics*, 2019, **10** (2), P. 164–175.
- [16] De la Rosa E., Diaz-Torres L.A., Salas P., Rodriguez R.A. Visible light emission under UV and IR excitation of rare earth doped  $\text{ZrO}_2$  nanophosphor. *Optical Materials*, 2005, **27**, P. 1320–1325.
- [17] Marin R., Sponchia G., et al. Monitoring the  $t \rightarrow m$  martensitic phase transformation by photoluminescence emission in  $\text{Eu}^{3+}$ -doped zirconia powders. *J. Am. Ceram. Soc.*, 2013, **96** (8), P. 2628–2635.
- [18] Manjunatha S., Dharmaprakash M.S.  $\text{Eu}^{3+}$  ion as a luminescent probe in  $\text{ZrO}_2\text{:Gd}^{3+}$  co-doped nanophosphor. *International Scholarly and Scientific Research & Innovation*, 2017, **11** (1), P. 56–59.
- [19] Ikeshita R., Hayakawa T., et al. Novel method to control initial crystallization of  $\text{Eu}^{3+}$  doped  $\text{ZrO}_2$  nanophosphors derived from a Sol Gel route based on  $\text{HNO}_3$  and their site-selective photoluminescence. *Journal of the Ceramic Society of Japan*, 2018, **126** (7), P. 551–556.
- [20] Zhang M., Zuo W., et al. Synthesis and photoluminescence properties of  $\text{Eu}^{3+}$ -doped  $\text{ZrO}_2$  hollow spheres. *J. Mater. Res.*, 2015, **30** (24), P. 3740–3745.
- [21] Bugrov A.N., Rodionov I.A., et al. Photocatalytic activity and luminescent properties of Y, Eu, Tb, Sm and Er-doped  $\text{ZrO}_2$  nanoparticles obtained by hydrothermal method. *Int. J. Nanotechnology*, 2016, **13** (1/2/3), P. 147–157.
- [22] Garcia-Hipolito M., Martinez E., et al. Preparation and characterization of Eu doped zirconia luminescent films synthesized by the pyrosol technique. *Journal of Materials Science Letters*, 2001, **20**, P. 1799–1801.
- [23] Wang M., Wang X., et al. Preparation and photoluminescence properties of  $\text{Eu}^{3+}$ -doped  $\text{ZrO}_2$  nanotube arrays. *Ceramics International*, 2015, **41** (7).
- [24] Colbea C., Avram D., et al. Full tetragonal phase stabilization in  $\text{ZrO}_2$  nanoparticles using wet impregnation: Interplay of host structure, dopant concentration and sensitivity of characterization technique. *Nanomaterials*, 2018, **8** (12), P. 988–1000.

- [25] Chen Guo, Peng Wang, et al. Morphology-Controllable Hydrothermal Synthesis of Zirconia with the Assistance of a Rosin-Based Surfactant. *Appl. Sci.*, 2019, **9**, 4145.
- [26] Bugrov A.N., Almjasheva O.V. Effect of hydrothermal synthesis conditions on the morphology of ZrO<sub>2</sub> nanoparticles. *Nanosystems: Physics, Chemistry, Mathematics*, 2013, **4** (6), P. 810–815.
- [27] Shu Z., Jiao X., Chen D. Synthesis and photocatalytic properties of flower-like zirconia nanostructures. *Cryst. Eng. Comm.*, 2012, **14** (1122).
- [28] Chen L., Liu Y., Li Y. Preparation and characterization of ZrO<sub>2</sub>:Eu<sup>3+</sup> phosphors. *Journal of Alloys and Compounds*, 2004, **381**, P. 266–271.
- [29] Sokolova M.P., Smirnov M.A., et al. Structure of composite based on polyheteroarylene matrix and ZrO<sub>2</sub> nanostars investigated by quantitative nanomechanical mapping. *Polymers*, 2017, **9** (7), P. 268.
- [30] Smith D., et al. Penn State University, University Park, Pennsylvania, USA, ICDD Grant-in-Aid, 1973.
- [31] Lin F.Q., Dong W.S., et al. In situ source – template-interface reaction route to hollow ZrO<sub>2</sub> microspheres with mesoporous shells. *Journal of Colloid and Interface Science*, 2008, **323**, P. 365–371.
- [32] Hecht H.G. The interpretation of diffuse reflectance spectra. *Journal of Research of the National Bureau of Standards - A. Physics and Chemistry*, 1976, **80A** (4), P. 567–583.
- [33] Heine C., Girgsdies F., et al. The model oxidation catalyst  $\alpha$ -V<sub>2</sub>O<sub>5</sub>: insights from contactless in situ microwave permittivity and conductivity measurements. *Appl. Phys. A*, 2013, **112** (2), P. 289–296.
- [34] Gallino F., Di Valentin C., Pacchioni G. Band gap engineering of bulk ZrO<sub>2</sub> by Ti doping. *Phys. Chem. Chem. Phys.*, 2011, **13**, P. 17667.
- [35] Li L., Yang H.K., et al. Structure, charge transfer bands and photoluminescence of nanocrystals tetragonal and monoclinic ZrO<sub>2</sub>:Eu. *Journal of Nanoscience and Nanotechnology*, 2011, **11**, P. 350–357.
- [36] Rao G.R., Sahu H.R. XRD and UV-Vis diffuse reflectance analysis of CeO<sub>2</sub>-ZrO<sub>2</sub> solid solutions synthesized by combustion method. *Proc. Indian Acad. Sci. (Chem. Sci.)*, 2001, **113** (5, 6), P. 651–658.
- [37] Bugrov A.N., Zavalova A.Yu., et al. Luminescence of Eu<sup>3+</sup> ions in hybrid polymer-inorganic composites based on poly(methyl methacrylate) and zirconia nanoparticles. *Luminescence*, 2018, **33** (5), P. 837–849.